Journal of Materials Chemistry C

PAPER

View Article Online
View Journal

Cite this: DOI: 10.1039/c4tc01692k

Molecular order of air-stable p-type organic thin-film transistors by tuning the extension of the π-conjugated core: the cases of indolo[3,2-*b*]-carbazole and triindole semiconductors†

Marta Reig,[a] Joaquim Puigdollers[b] and Dolores Velasco*[a]

Received 31st July 2014
Accepted 1st October 2014

DOI: 10.1039/c4tc01692k

www.rsc.org/MaterialsC

Charge transport in organic devices depends strongly on the molecular order and morphology of the organic semiconductor thin films. In the design of new organic semiconductors, the selection of the appropriate core plays a key role in the molecular packing and charge transport characteristics of the organic device. Four derivatives of carbazole that mainly differ in the extension of the π-conjugated core, including indolo[3,2-*b*]carbazole and triindole derivatives, exhibited hole mobilities ranging from 10^{-5} to 10^{-2} cm^2 V^{-1} s^{-1} as active layers in organic thin-film transistors (OTFTs). X-ray analyses of the single crystals and evaporated thin films gave insights into the molecular packing of the compounds that justified their OTFTs characteristics.

Introduction

After intensive research effort, p-type OTFTs have now successfully achieved hole mobilities comparable to those obtained with amorphous silicon. The performances of OTFTs have achieved impressive progress in recent years, due to the processing of new materials, device geometries, and morphology control. However, the properties of the organic semiconductors still determine the performance of OTFT devices. In view of this, when designing new suitable organic compounds for molecular electronics, the selection of an appropriate core structure is a significant aspect to take into account,[1] because it could modulate the optical and electronic properties and even determine the stability and durability of the fabricated devices under ambient conditions. One strategy to achieve materials with high air stability is to work with compounds that exhibit low-lying high occupied molecular orbital (HOMO) levels, in order to obtain compounds stable against oxidative doping by atmospheric oxygen.

The search for high mobility organic semiconductors has yielded pentacene as one of the most promising materials, achieving high hole mobilities of 3 cm^2 V^{-1} s^{-1} for vacuum deposited OTFTs.[1b,2] Nevertheless, pentacene-based devices present several drawbacks for practical applications due to a lack of air stability and fast device degradation.[3]

Carbazole derivatives have been widely studied as hole-transporting semiconductors, due to their electron-donating capabilities.[4] In addition, they are recognised as reasonably stable compounds against oxidative doping by atmospheric oxygen. The carbazole unit presents a series of advantages ahead of other conventional organic semiconductors, such as its low cost, easy availability, and its high stability in environmental conditions.

In this work, we deal with the study of 9-methyl-9*H*-carbazole **1**, 9,9′-dimethyl-9*H*,9*H*′-[3,3′]bicarbazole **2**, 5,11-dimethylindolo-[3,2-*b*]carbazole **3**, and *N*-trimethyltriindole **4** (Fig. 1) as active organic semiconductor layers in OTFTs. Within this

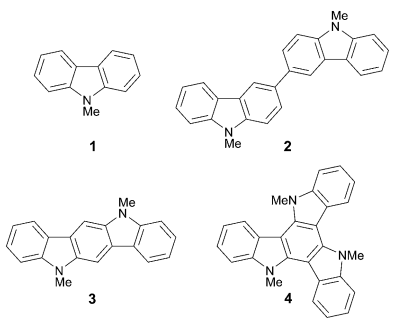

Fig. 1 Molecular structure of carbazole-based derivatives **1**–**4**.

[a]*Grup de Materials Orgànics, Institut de Nanociència i Nanotecnologia (IN²UB), Departament de Química Orgànica, Universitat de Barcelona, Martí i Franquès 1, E-08028, Barcelona, Spain. E-mail: dvelasco@ub.edu; Fax: +34 93 339 78 78; Tel: +34 93 403 92 60*

[b]*Dept. Eng. Electrònica & Centre de Recerca en Nanoenginyeria, Universitat Politècnica de Catalunya, C/Jordi Girona, 1-3, 08034, Barcelona, Spain. E-mail: joaquim.puigdollers@upc.edu; Tel: +34 93 401 10 02*

† Electronic supplementary information (ESI) available: Absorption spectra, cyclic voltammograms, OTFTs characteristics, detailed crystallographic data and powder X-ray diffraction patterns. CCDC 1017245. For ESI and crystallographic data in CIF or other electronic format see DOI: 10.1039/c4tc01692k

series, the extension of the π-conjugated core was progressively varied, leading to improved OTFTs performances of 10^{-2} cm^2 V^{-1} s^{-1}.

Indolo[3,2-*b*]carbazole and triindole show extended π systems, in which two or three carbazole units, respectively, share an aromatic ring. Indolo[3,2-*b*]carbazole and triindole unit present a planar structure with two or three N–H units, respectively, which allows easy introduction of alkyl chains, in order to increase the solubility of the systems and to promote the molecular order of the materials during the deposition process. Both heterocycles display large energy band gaps and low-lying HOMO energy levels. In the last few years, indolocarbazole has received special attention as a building block in the field of organic electronics, and recent studies have shown the great potential of indolo[3,2-*b*]carbazole-based derivatives to be used in OTFTs.[5] The triindole core presents a larger molecular structure than the indolocarbazole core. Accordingly, a higher molecular order could be expected from it, and therefore, better charge carrier transport. To the best of our knowledge, there are still no studies about the application of triindole derivatives in OTFTs. Recently, triindole derivatives have been described as suitable organic materials in Organic Solar Cells (OSCs)[6] and OLEDs.[7] The charge transport properties of liquid-crystal-based triindole derivatives[8] and of triindole **4** have been reported by the space-charge-limited-current method (SCLC), yielding values of hole mobilities for the later ranging from ~1 × 10^{-4} to ~1 × 10^{-3} cm^2 V^{-1} s^{-1}.[6b] The easy preparation, high thermal stability, π-stacking capability, high carrier mobilities, and optoelectronic properties of such molecules make indolocarbazole- and triindole-based materials very promising organic semiconductors for optoelectronic applications.

Here, we report not only the OTFT performance of carbazole containing compounds **1–4**, but also the determination of the molecular packing in the organic semiconductor layer of the devices by means of X-ray diffraction (XRD) studies. Therefore, the aim of this work is to determine the correlation of the device performance with the molecular order in the semiconducting thin films as a function of the π-conjugated core design of the organic semiconductors.

Results and discussion

Synthesis and physical properties

Compound **2** was synthesized by oxidative dimerization of 9-methyl-9*H*-carbazole with $FeCl_3$ in anhydrous chloroform following a previously reported procedure.[9] Indolo[3,2-*b*]carbazole was synthesized by condensation of 1,4-cyclohexanodione with phenylhydrazine, followed by a double Fischer indolization.[10] Triazatruxene was synthesized by the cyclocondensation of 2-oxindole.[11] *N*-methyl derivatives **1**, **3** and **4** of the corresponding 9*H*-carbazole, indolo[3,2-*b*]carbazole, and triazatruxene were obtained by methylation under standard conditions in high yields. Compounds **1–4** were entirely characterized by ^{1}H-NMR, ^{13}C-NMR and MS.

Indolocarbazole **3** and triindole **4** exhibited high thermal stability by thermal gravimetric analysis (TGA), showing the onset of decomposition at 384 °C and 461 °C, respectively.

Compounds **1–4** showed one oxidation process by cyclic voltammetry, whereas no reduction processes were observed for any of them. Table 1 collects the electrochemical characteristics, the HOMO energy level estimated from cyclic voltammetry and the energy band gap estimated from the UV-visible spectra (the absorption spectra and cyclic voltammograms can be found in the ESI, Fig. S1 and S2†). In this series of carbazole-based compounds, when increasing the conjugation of the system, the HOMO levels are slightly destabilized from −6.16 eV for carbazole **1** to −5.45 eV corresponding to triindole derivative **4** (Fig. 2). The relative low-lying HOMO levels and high HOMO–LUMO gaps (~3.7 eV) of these compounds are indicative of their potential hole transporting properties. Moreover, the energy levels found for the organic semiconductors **1–4** are perfectly suitable to Au electrode work function (−5.1 eV) as it is displayed in Fig. 2.

Organic thin-film transistors

Charge carrier mobilities were measured by using the organic materials **1–4** as vacuum-deposited active layers in standard bottom gate-top contact OTFTs.

The fabrication of OTFTs with compound **1** as the organic semiconductor layer was not successful, due to its low sublimation temperature (40 °C at 10^{-6} mbar under the experimental conditions during the deposition process). **2**-based devices fabricated with 50 nm thick SiO_2 dielectric presented a bad yield and poor reproducibility: only 17% of the devices fabricated with polystyrene (PS) treated substrates presented OTFT characteristics, with a maximum hole mobility around 2 × 10^{-5} cm^2 V^{-1} s^{-1} and a threshold voltage of −16.0 V (Table 1).

Table 1 presents the device characterization for OTFTs fabricated with the more extended π-conjugated cores of compounds **3** and **4**. Devices fabricated with substrates of 50 nm of SiO_2 presented similar hole mobilities, but lower threshold voltages, than those fabricated from substrates of 110 nm of SiO_2. The reproducibility of the measurements and the yield of the working devices were found to be independent of the thickness of the SiO_2 layer. The highest values of charge mobilities were achieved by modifying the dielectric surface with a polystyrene thin film layer, which also resulted in lower threshold voltages and a higher reproducibility. **3** and **4** PS-treated SiO_2 devices presented a superior yield, as given by the average of ten devices (**3**: 89% and **4**: 100%), exhibiting all of the tested devices with similar performances. The highest hole mobility was registered for triindole **4**, 3 × 10^{-2} cm^2 V^{-1} s^{-1} in front of 7 × 10^{-3} cm^2 V^{-1} s^{-1} for the indolocarbazole **3**. The OTFTs characteristics of **3**- and **4**-based devices fabricated on bare SiO_2 surfaces showed lower reproducibility and lower charge mobilities of 7 × 10^{-5} and 5 × 10^{-3} cm^2 V^{-1} s^{-1}, respectively.

A representative output, transfer, and saturation characteristics for 4-based OTFTs are shown in Fig. 3 (Fig. 3a and b; for OTFT characteristics of compound **3**-based devices see ESI, Fig. S3a and b†). The output characteristics are indicative of the OTFT behaviour of the device in both the linear and saturated

Table 1 Optical and electrochemical properties for compounds **1–4** and OTFT characteristics of devices based on **1–4** carbazole derivatives with polystyrene treated c-Si/SiO_2 substrates

Compound	λ_{abs} (ε)[a] nm (M^{-1} cm^{-1})	E_{onset}^{ox}[b] (V)	E_{gap}[c] (eV)	E_{HOMO}/E_{LUMO} (eV)	μ (cm^2 V^{-1} s^{-1})	V_{th} (V)	I_{on}/I_{off} (A/A)
1	263 (32 314), 294 (29 722)	1.20	4.10	−6.16/−2.06	—	—	—
2	303 (76 660)	0.84	3.90	−5.80/−1.90	2×10^{-5}	−16.0	$\sim 10^1$
3	283 (52 268), 340 (67 146)	0.68	3.57	−5.64/−2.07	7×10^{-3} (1×10^{-3})[e]	−9.6 (−5.5)[e]	$\sim 10^4$
4	317 (79 023)	—	3.53	−5.45[d]/−1.92	3×10^{-2} (1×10^{-2})[f]	−12.8 (−9.0)[f]	$\sim 10^3$

[a] Wavelength of the maximum absorption and molar extinction coefficient. [b] Onset oxidation potential. [c] Energy difference between the HOMO and LUMO orbitals. [d] Determined from data given in ref. 6b. [e] Maximum value registered on the 8th day. [f] Maximum value registered on the 5th day. The results in parentheses are for the measurements after five months in air.

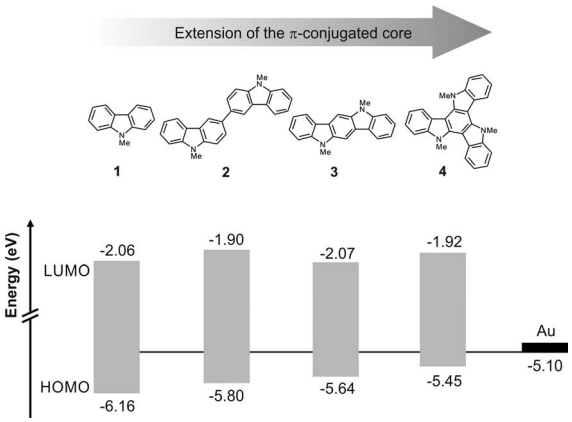

Fig. 2 Energy levels (HOMO–LUMO) of materials **1–4** measured by cyclic voltammetry. Gold is also shown for comparison.

regions. The hole mobility (μ) in the saturated region and the threshold voltage (V_{th}) were calculated from eqn (1):

$$I_D = \frac{WC_{ox}\mu}{2L}(V_G - V_{th})^2 \quad (1)$$

where W and L are the channel width and length, respectively, C_{ox} is the unit dimensional dielectric capacitance of gate insulator, μ is the hole mobility and V_{th} is the threshold voltage.

A key requirement in the design of new semiconductors is the stability under ambient conditions. OTFTs fabricated with both types of semiconductors **3** and **4** operate well in air, exhibiting remarkable ambient storage stability. Similar threshold voltages, mobilities and I_{on}/I_{off} ratios were obtained after 5 months of storage in air and in dark conditions, demonstrating excellent air stability (Fig. 3c and d, the air-stability experiments for **3**-based devices can be found in the ESI, Fig. S3c and d†). The increase in charge mobilities after the first few days of exposure to air can be attributed to p-doping of the device by O_2.

Molecular order and morphology of the thin films

For further exploration of the relationship between the OTFTs performance and the role of the molecular order in the thin films, grazing incidence X-ray diffraction (GIXRD) and atomic force microscopy (AFM) analysis were performed.

First of all, the knowledge of the single crystal structure of compounds **3** and **4** was crucial because it could provide the molecular packing motif and indicate the main intermolecular interactions of these compounds. The crystal structure of triindole derivative **4** was previously reported[12] to adopt a face-to-face packing in an alternate arrangement due to the π–π interactions between adjacent triindole molecules. For that compound, two different distances (3.53 Å and 3.68 Å) between two neighbouring molecules were observed due to the steric hindrance induced by the methyl groups.

In order to examine the molecular packing and the intermolecular interactions in the indolocarbazole derivative **3**, the single crystal structure was determined by X-ray crystallography. The compound crystallizes in space group C2/c of the monoclinic system with unit-cell dimensions of $a = 16.8377(13)$ Å, $b = 5.6889(4)$ Å, $c = 15.3882(11)$ Å, $\beta = 106.671°(2)$, and volume = 1412.05(18) $Å^3$. The cif file and the detailed crystallographic data are provided in the ESI (Table S1–S5 and Fig. S4†).

The X-ray structure of **3** is shown in Fig. 4. The molecular structure of indolocarbazole **3** is nearly planar, with a small torsion angle around 1.5° (Fig. 4a). The molecules exhibit a herringbone packing motif with a herringbone angle of 70.96° (Fig. 4b). Every molecule is surrounded by six molecules showing C–H···π interactions between one of the hydrogen atoms of the methyl groups with the central benzene ring of an adjacent indolocarbazole molecule with a distance of 2.68 Å. Moreover, one of the hydrogen atoms of the methyl groups also interacts with one peripheral benzene ring with a distance of 3.01 Å, being responsible for the abovementioned herringbone packing motif (Fig. 4c).

For indolo[3,2-*b*]carbazole derivatives, the packing motif in the solid state strongly depends on the length of the alkyl chain in the nitrogen position of the indolocarbazole derivatives. Different packing motifs have been described in previously reported methods, from the non-substituted indolo[3,2-*b*]carbazole[13] to alkylated derivatives.[13,14] For GIXRD studies, 75 nm thick films were deposited by sublimation in a vacuum system of compounds **3** and **4** on both bare and on polystyrene treated c-Si/SiO_2 surfaces. All the thin films showed strong diffraction peaks, which suggested that both **3** and **4** produced well-ordered films under the experimental conditions (Fig. 5). As shown in Fig. 5a, vacuum deposited **3** thin films on bare and on PS-treated c-Si/SiO_2 surfaces presented identical X-ray diffraction patterns, which means that the molecules are

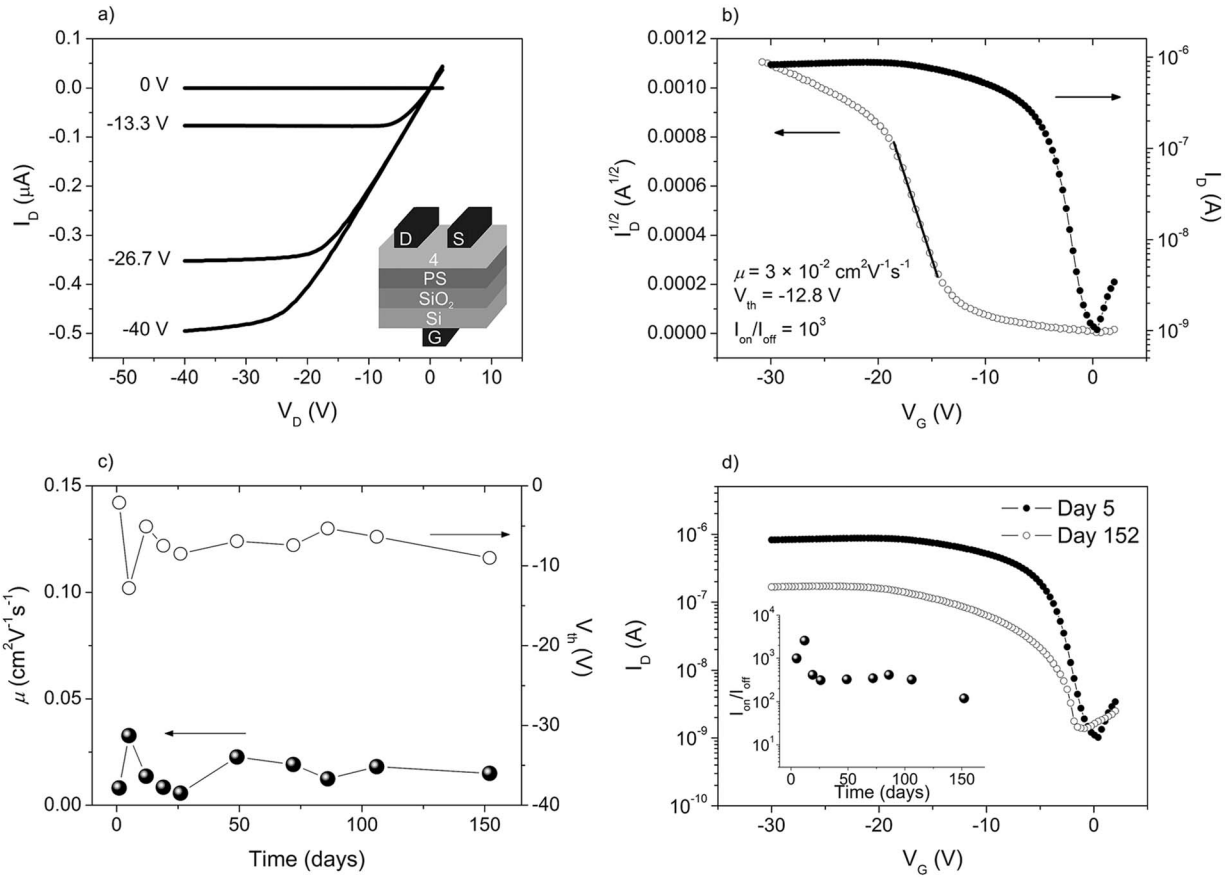

Fig. 3 OTFTs characteristics of a device fabricated with **4** as the semiconductor layer and with PS-treated substrate. (a) Output characteristics at different gate voltages (V_G). (b) Transfer ($V_D = -20$ V) and saturation characteristics. (c) Mobility and threshold voltage of one representative device fabricated with **4** as the semiconductor layer and with PS-treated substrate as a function of storage time in the air. (d) Transfer characteristics on the 5th day and the 152nd day of the experiment at $V_D = -20$ V. Inset figure shows the evolution with time of the I_{on}/I_{off} ratio of the selected device.

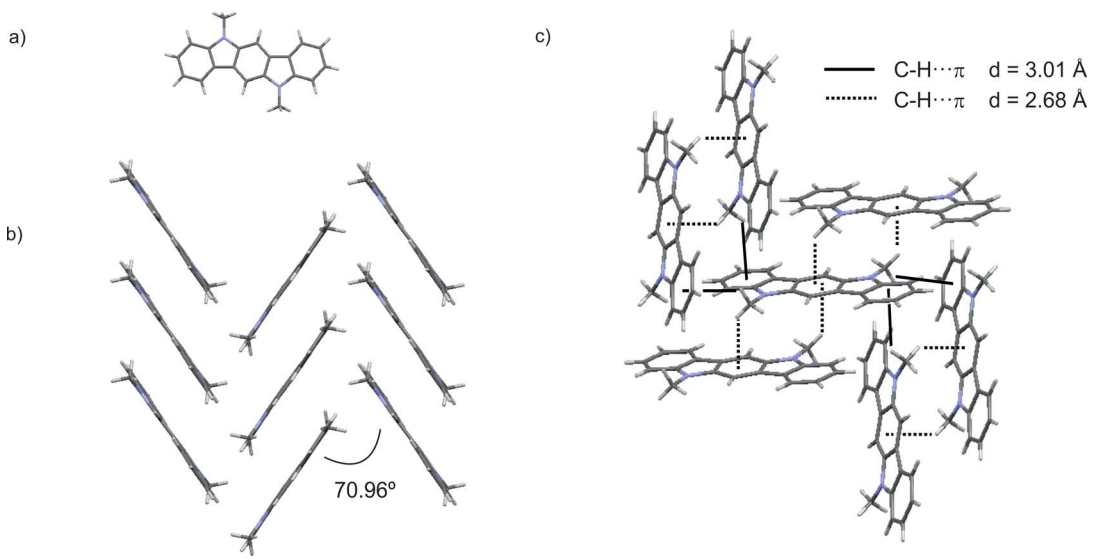

Fig. 4 Single crystal structure of compound **3**. (a) Molecular structure, (b) herringbone packing motif with its corresponding herringbone angle and (c) short contacts given by C–H···π interactions.

equally oriented, both on bare and on PS-treated SiO_2 surfaces. The combination of the GIXRD studies with the powder XRD data and the single crystal structures provides valuable information about the molecular order in the thin films.[13,15]

Thin films based on indolocarbazole **3** presented only one strong diffraction peak in the GIXRD patterns at $2\theta = 11.1°$, in comparison to the more complex diffractogram spectra obtained from the powder XRD data (Fig. S5a† in the ESI). From the single crystal data and the powder XRD pattern, the diffraction peak at $2\theta = 11.1°$ can be undoubtedly assigned to the reflection 200. The XRD study shows that the plane (100) is parallel to the c-Si/SiO_2 substrate, *i.e.* with *b*- and *c*-axis also in the parallel plane. The molecular packing within the thin film corresponds to that of indolocarbazole **3** in the single crystal. This suggests that the molecules are tilted with an angle of 68° to the substrate (Fig. 5a and b).

For vacuum deposited **4** thin films on PS-treated substrates, one diffraction peak was mainly observed in the thin film XRD pattern at $2\theta = 8.3°$, together with a second order diffraction peak at $2\theta = 16.6°$, which is indicative of a higher crystalline thin film than that obtained for indolocarbazole **3**. From the single crystal data,[12] the powder XRD pattern (Fig. S5b† in the ESI) and the GIXRD data, the diffraction peaks at $2\theta = 8.3°$ and $2\theta = 16.6°$ were assigned to the corresponding reflections 110 and 220, respectively, suggesting that they are parallel to the substrate with the *c*-axis also in the parallel plane. Consequently, as it is collected in Fig. 5c, triindole molecules are located totally perpendicular (90°) to the substrate surface.

For the OTFTs performance, the best charge carrier mobility was found for the triindole derivative **4**-based devices in comparison with those obtained from the indolocarbazole **3**. This improvement in the charge carrier mobility value can be related to the different packing motifs and the corresponding different intermolecular interactions, and with the different molecular order in the thin films. From the single crystal data reported above, it can be established that a change in the packing motif exists from the herringbone of compound **3** with $CH_3\cdots\pi$ interactions to a face-to-face arrangement of compound **4**, dominated by π–π interactions, in which the electronic coupling is maximized and the charge transport should be favoured. As a second important point, the GIXRD suggests that molecules in **4** are located completely perpendicular to the substrate, which seems to be the best molecular disposition for the charge transport through the semiconductor active layer of an OTFT with a bottom-gate top-contact geometry.

In addition to the local intermolecular interactions, the film morphology and the grain sizes and boundaries strongly influence the charge transport properties, particularly at the interface between the semiconductor and the dielectric. AFM images were taken from the **3** and **4** films deposited by sublimation on both bare and polystyrene treated SiO_2 surfaces (Fig. 6). Remarkable morphology differences were observed between them.

Thin films based on indolocarbazole **3** deposited on bare SiO_2 and on PS-treated surfaces showed similar topography profiles. Both films present a similar average grain size, with an average width of 600 nm and lengths that include from 600–1400 nm. Only a slight enhancement of the interconnectivity between the grains is observed for films based on **3** deposited on PS-treated surfaces, which actually correspond to a higher device performance (Fig. 6a and b, Table 1). Vacuum-deposited

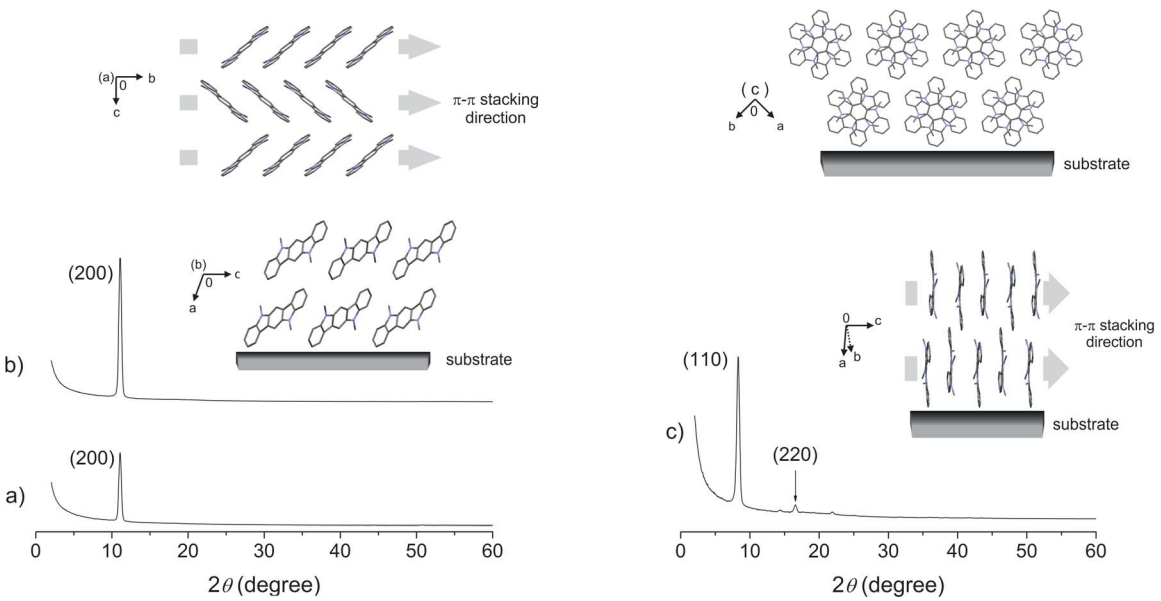

Fig. 5 GIXRD patterns of vacuum-deposited **3** films on (a) bare and (b) polystyrene-treated c-Si/SiO_2 surfaces. The inset image shows the molecular packing of compound **3** with the (100) plane situated at 27° (above) and perpendicular (below) to the paper plane, respectively. (c) GIXRD pattern of vacuum-deposited **4** film on a polystyrene-treated c-Si/SiO_2 surface. The inset images show the molecular packing in the thin films seen from two different perspectives, being the (110) plane situated perpendicular to the paper. The hydrogen atoms were omitted for clarity.

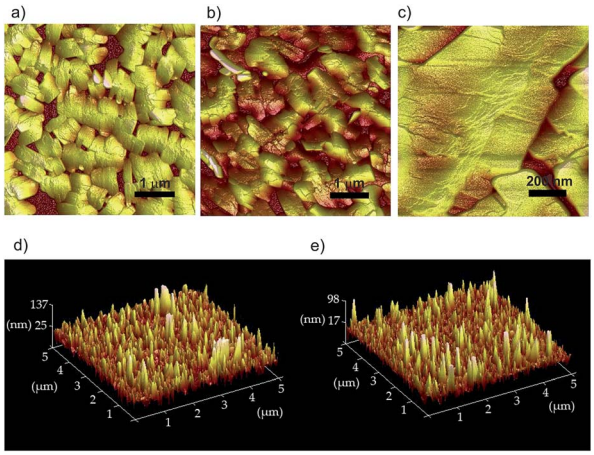

Fig. 6 AFM images of vacuum-deposited **3** films deposited on (a) bare SiO_2 (5×5 μm^2), (b) polystyrene treated SiO_2 (5×5 μm^2) and (c) polystyrene treated SiO_2 (1×1 μm^2). AFM images of vacuum-deposited **4** films deposited on (d) bare SiO_2 (5×5 μm^2) and (e) polystyrene treated SiO_2 (5×5 μm^2).

3 films presented a terrace-like step morphology (Fig. 6c), independent of the modification of the dielectric surface.

Vacuum-deposited **4** films on bare and on PS-treated SiO_2 also presented identical morphologies, independently of the modification of the dielectric surface (Fig. 6d and e). AFM images exhibited protrusions/hillocks, whose average thickness was in the order of 130 nm and their height varied from 50 nm to more than 100 nm.

Combining GIXRD and AFM data, it can be established that vacuum deposited films of indolocarbazole **3** and triindole **4** derivatives on bare and on PS-treated SiO_2 surfaces, respectively, presented identical X-ray diffraction patterns and morphology. Therefore, the addition of a polystyrene SAM has a null influence on the growth of the molecular order and on the morphology of the thin film. The improvement of the electrical characteristics of the OTFT devices observed in PS-treated c-Si/SiO_2 substrates appears to be related to the improvement of the interface contact between the dielectric and the semiconductor layer.

Experimental section

Materials

All reagents for syntheses were obtained from commercial sources and were used as received without further purification. Indolo[3,2-*b*]carbazole was synthesized according to previously reported method.[10] Triazatruxene was synthesized according to a previously reported method.[11]

Synthesis of 9,9′-dimethyl-9*H*,9*H*′-[3,3′]bicarbazole (2)

9-Methyl-9*H*-carbazole **1** (5.6 g, 31.1 mmol) was dissolved in anhydrous $CHCl_3$ (70 mL) under an inert atmosphere. Subsequently, $FeCl_3$ (13.7 g, 84.5 mmol) was added and the reaction mixture was stirred at room temperature for 30 minutes. Then, the mixture was poured into methanol and the formation of a precipitate was observed. The solid was isolated by vacuum filtration, washed thoroughly with methanol and then dried. The crude was purified by flash column chromatography using a mixture of hexane and CH_2Cl_2 (1 : 1 v/v) as eluent to give compound **2** (4.3 g, 73%). ^{1}H NMR (400 MHz, d_6-DMSO), δ: 8.55 (d, $J = 1.7$ Hz, 2H), 8.26 (d, $J = 7.6$ Hz, 2H), 7.89 (dd, $J = 8.5$ Hz, $J = 1.7$ Hz, 2H), 7.67 (d, $J = 8.5$ Hz, 2H), 7.58 (d, $J = 8.2$ Hz, 2H), 7.50–7.46 (m, 2H), 7.24–7.21 (m, 2H), 3.92 (s, 6H, N–CH_3) ppm. ^{13}C NMR (100 MHz, d_6-DMSO), δ: 141.1, 139.7, 132.2, 125.8, 125.0, 122.7, 122.3, 120.4, 118.7, 118.2, 109.4, 109.2, 29.1 ppm. HRMS (ESI-MS) (m/z): calcd for $C_{26}H_{21}N_2$ $(M + H)^+$ 361.1699, found: 361.1684.

Synthesis of 5,11-dimethylindolo[3,2-*b*]carbazole (3)

NaH (12 mg, 0.52 mmol) was added to a solution of indolo[3,2-*b*]carbazole (60 mg, 0.23 mmol) in anhydrous DMF under an inert atmosphere. The solution was stirred at room temperature for 30 minutes. Then, methyl iodide (32 μL, 0.52 mmol) was added and the mixture was stirred at room temperature for 30 minutes and then treated with H_2O. The aqueous layer was extracted with dichloromethane and the organic layer was dried over Na_2SO_4. The solvent was removed by evaporation and the crude was purified by flash column chromatography using a mixture of hexane and dichloromethane (4 : 1 v/v) to give compound **3** (55 mg, 83%).^{1}H NMR (400 MHz, $CDCl_3$), δ: 8.20 (d, $J = 8.0$ Hz, 2H), 8.02 (s, 2H), 7.53–7.49 (m, 2H), 7.42 (d, $J = 8.0$ Hz, 2H), 7.26–7.22 (m, 2H), 3.96 (s, 6H, N–CH_3) ppm. ^{13}C NMR (100 MHz, $CDCl_3$), $\delta = 142.3$, 136.9, 125.8, 123.0, 122.9, 120.3, 118.2, 108.3, 98.7, 29.5 ppm. HRMS (ESI-MS) (m/z): calcd for $C_{20}H_{17}N_2$ $(M + H)^+$ 285.1386, found: 285.1382.

Synthesis of *N*-trimethyltriindole (4)

NaH (98 mg, 4.05 mmol) was added to a solution of triazatruxene (0.28 g, 0.81 mmol) in anhydrous DMF under an inert atmosphere. The solution was stirred at room temperature for 30 minutes. Then, methyl iodide (166 μL, 2.67 mmol) was added and the mixture was stirred at room temperature for 30 minutes and then treated with H_2O. The aqueous layer was extracted with dichloromethane and the organic layer was dried over Na_2SO_4. The solvent was removed by evaporation and the crude was purified by flash column chromatography using a mixture of hexane and dichloromethane (5 : 1 v/v) as eluent to give compound **4** (0.26 g, 84%). ^{1}H NMR (400 MHz, $CDCl_3$), δ: 8.47 (d, $J = 8.0$ Hz, 3H), 7.59 (d, $J = 8.0$ Hz, 3H), 7.49–7.45 (m, 3H), 7.37–7.33 (m, 3H), 4.48 (s, 9H, N–CH_3) ppm. ^{13}C NMR (100 MHz, $CDCl_3$), $\delta = 142.1$, 139.2, 123.0 (2C), 121.9, 120.0, 109.8, 102.7, 36.1 ppm. HRMS (ESI-MS) (m/z): calcd for $C_{27}H_{22}N_3$ $(M + H)^+$ 388.1808, found: 388.1810.

Instrumentation and methods

Flash column chromatography was carried out over silica gel (SDS, 230–240 mesh). ^{1}H NMR (400 MHz) and ^{13}C NMR (100 MHz) spectra were collected on a Varian Mercury spectrophotometer. NMR spectra were processed with the MestRec Nova software. HRMS was performed using a LC/MSD-TOF Agilent Technologies apparatus by electrospray (ESI-MS)

technique. UV-Vis spectra were registered using a Varian Cary UV-Vis-NIR 500E spectrophotometer. TGA were performed with a Mettler Toledo TGA/SDTA 851e instrument at a heating rate of 10 K min^{-1}. Differential scanning calorimetry (DSC) thermograms were recorded using a Mettler–Toledo DSC821 module under a nitrogen flow. Cyclic voltammograms were carried out using a microcomputer-controlled potentiostat/galvanostat Autolab with PGSTAT30 equipment and GPES software. A cylindrical three-electrode cell was used. The reference electrode was a Metrohm Ag/AgCl/KCl (3 M) mounted in a Luggin capillary containing a 0.1 M solution of tetrabutylammonium perchlorate (TBAP) in dichloromethane. The counter and working electrodes were a platinum spiral and a platinum wire, respectively. All voltammetric curves were recorded under quiescent conditions, at a scan rate of 100 mV s^{-1} and under an argon atmosphere. All solutions were prepared in dichloromethane (1 mM). Tetrabutylammonium perchlorate (Aldrich, electrochemical grade) was used as a supporting electrolyte. The energy of the HOMO level was estimated from the onset of the first oxidation peak as $E_{HOMO} = -E^{ox}_{onset} + E^{0}(Fc/Fc^{+}) - 5.39$, where $E^{0}(Fc/Fc^{+}) = +0.19$ V *vs.* Ag/AgCl/KCl (3 M), and where −5.39 eV corresponds to the formal potential of the Fc^{+}/Fc redox couple in the Fermi scale.[16] The energy of the LUMO level was calculated as $E_{LUMO} = E_{HOMO} + E_{gap}$. Single-crystal analysis of material **3** was performed on a D8 Venture system equipped with a multilayer monochromator and a Mo high brilliance Incoatec Microfocus Source ($\lambda = 0.71073$ Å). The frames were integrated with the Bruker SAINT software package using a narrow-frame algorithm. The structure was solved and refined using the Bruker SHELXTL Software Package. Powder X-ray diffraction (XRD) measurements were obtained using a PANalytical X'Pert PRO MPD θ/θ powder diffractometer, in a configuration of a convergent beam with a focalizing mirror and transmission geometry with a spinner glass capillary sample holder, a PIXcel detector and with Cu Kα radiation at 45 kV and 40 mA. Samples were prepared by introduction of the powder materials **3** and **4** in Lindemann glass capillaries of 0.5 millimetres of diameter. Grazing incidence XRD (GIXRD) measurements of the thin-films of the sublimated organic materials were performed using a PANalytical X'Pert PRO MRD diffractometer with a PIXcel detector, a parabolic Göbel mirror at the incident beam and a parallel plate collimator at the diffracted beam, and with Cu Kα radiation at 45 kV and 40 mA. The angle of incidence used was $\omega = 0.17°$. Thin films (75 nm) were prepared from compounds **3** and **4** by sublimation on a vacuum system on a c-Si/SiO_2 substrate and on polystyrene-treated c-Si/SiO_2 substrates with a deposition rate of 0.3 Å s^{-1} under a pressure below 10^{-6} mbar. AFM experiments were conducted using an AFM Dimension 3100 system attached to a Nanoscope IVa electronics unit (Bruker).

OTFT device fabrication

OTFTs devices were fabricated using the bottom-gate top-contact geometry. The substrate present in a thermally oxidized crystalline silicon wafer provided a gate dielectric (SiO_2) of a thickness of 50 nm and 110 nm. Polystyrene (PS) was used as a self-assembled monolayer to improve the device performance. A solution of PS in toluene (4 mg mL^{-1}) was deposited drop wise on the substrate. The substrate was spun at 500 rpm for 5 s and 2500 rpm for 30 s with a P6700 spin coater. Organic materials **2**–**4** were deposited by sublimation in a vacuum system with a base pressure below 10^{-6} mbar. The sublimation temperature for the organic compounds was regulated from 152 to 160 °C, 120 to 130 °C and 160 to 170 °C, respectively, to maintain a stable deposition rate around 0.3 Å s^{-1} to obtain a 75 nm thickness layer. Then, they were transferred to a different vacuum chamber to evaporate the metallic contacts. Gold was used for the source and drain electrodes, which were defined using a metallic mask that defines a channel length (L) and width (W) of 80 μm and 2 mm, respectively. The fabricated OTFTs were electrically characterized in the dark and under air conditions. The electrical characteristics were measured using an Agilent 4156C parameter analyser.

Conclusions

All the carbazole-based compounds **1**–**4** presented low HOMO levels and high HOMO–LUMO gaps, indicating their potential hole-transporting properties and air-stability. However, only compounds **3** and **4**, with extended π-conjugated cores with two and three fused carbazole rings, presented good device performances and air-stability and durability under air conditions, for longer periods of up to 5 months, with hole mobility values ranging from 10^{-3} to 10^{-2} cm^2 V^{-1} s^{-1}. For indolocarbazole derivative **3**, a herringbone packing motif with $CH_3\cdots\pi$ interactions has been described in the semiconductor layer, whereas a cofacial molecular packing is observed for triindole **4**. For the latter, it has been found that in the crystal structure and in the thin film, it presents a face-to-face molecular packing, and exhibits the best OTFT performance. For this material, an optimal perpendicular molecular disposition to the substrate surface was determined by GIXRD. Indolo[3,2-*b*]carbazole and specially triindole units are shown to be promising π-conjugated cores for new organic semiconductors for electronic devices.

Acknowledgements

Financial support from the *Ministerio de Economía y Competitividad* (CTQ2012-36074 and TEC2011-27859) is gratefully acknowledged. M. Reig is grateful for the grant ADR from *Universitat de Barcelona* (UB). We also thank Xavier Alcobé and Josep M^{a} Bassas from the X-ray diffraction unit of the Scientific and Technological Centers of the University of Barcelona (CCiTUB) for the realization of the X-ray diffraction measurements and their helpful discussion.

Notes and references

1 (*a*) R. Fitzner, E. Mena-Osteritz, A. Mishra, G. Schulz, E. Reinold, M. Weil, C. Körner, H. Ziehlke, C. Elschner, K. Leo, M. Riede, M. Pfeiffer, C. Uhrich and P. Bäuerle, *J. Am. Chem. Soc.*, 2012, **134**, 11064; (*b*) J. Mei, Y. Diao,

A. L. Appleton, L. Fang and Z. Bao, *J. Am. Chem. Soc.*, 2013, **135**, 6724.

2 (*a*) M. E. Roberts, S. C. B. Mannsfeld, N. Queraltó, C. Reese, J. Locklin, W. Knoll and Z. Bao, *Proc. Natl. Acad. Sci. U. S. A.*, 2008, **105**(34), 12134; (*b*) H. Klauk, M. Halik, U. Zschieschang, G. Schmid, W. Radlik and W. Weber, *J. Appl. Phys.*, 2002, **92**, 5259.

3 (*a*) D. Simeone, S. Cipolloni, L. Mariucci, M. Rapisarda, A. Minotti, A. Pecora, M. Cuscunà, L. Maiolo and G. Fortunato, *Thin Solid Films*, 2009, **517**, 6283; (*b*) K. Takimiya, T. Yamamoto, H. Ebata and T. Izawa, *Sci. Technol. Adv. Mater.*, 2007, **8**, 273.

4 (*a*) S. Castellanos, V. Gaidelis, V. Jankauskas, J. Grazulevicius, E. Brillas, F. López-Calahorra, L. Juliá and D. Velasco, *Chem. Commun.*, 2010, **46**, 5130; (*b*) A. Tomkeviciene, J. V. Grazulevicius, D. Volyniuk, V. Jankauskas and G. Sini, *Phys. Chem. Chem. Phys.*, 2014, **16**, 13932; (*c*) Y. M. Tao, H. Y. Li, Q. L. Xu, Y. C. Zhu, L. C. Kang, Y. X. Zheng, J.-L. Zuo and X. Z. You, *Synth. Met.*, 2011, **161**, 718; (*d*) P. Sigwalt, G. Wegner, J.-F. Morin, M. Leclerc, D. Adès and A. Siove, *Macromol. Rapid Commun.*, 2005, **26**, 761.

5 (*a*) H. Zhao, L. Jiang, H. Dong, H. Li, W. Hu and B. S. Ong, *ChemPhysChem*, 2009, **10**, 2345; (*b*) P.-L. T. Boudreault, S. Wakim, M. L. Tang, Y. Tao, Z. Bao and M. Leclerc, *J. Mater. Chem.*, 2009, **19**, 2921.

6 (*a*) X. Qian, Y.-Z. Zhu, J. Song, X.-P. Gao and J.-Y. Zheng, *Org. Lett.*, 2013, **15**(23), 6034; (*b*) S. W. Shelton, T. L. Chen, D. E. Barclay and B. Ma, *ACS Appl. Mater. Interfaces*, 2012, **4**, 2534.

7 (*a*) D. H. Huh, G. W. Kim, G. H. Kim, C. Kulshreshta and J. H. Kwon, *Synth. Met.*, 2013, **180**, 79; (*b*) W. Y. Lai, Q. Y. He, R. Zhu, Q. Q. Chen and W. Huang, *Adv. Funct. Mater.*, 2008, **18**, 265.

8 E. M. García-Frutos, U. K. Pandey, R. Termine, A. Omenat, J. Barberá, J. L. Serrano, A. Golemme and B. Gómez-Lor, *Angew. Chem., Int. Ed.*, 2011, **50**, 7399.

9 (*a*) V. Vaitkeviciene, S. Grigalevicius, J. V. Grazulevicius, V. Jankauskas and V. G. Syromyatnikov, *Eur. Polym. J.*, 2006, **42**, 2254; (*b*) T. Tokuda, K. Murashiro, M. Kubo, H. Masu, M. Imanari, H. Seki, N. Aoki, Y. Ochiai, H. Kanoh and K. Hoshino, *Langmuir*, 2012, **28**, 16430.

10 B. Robinson, *J. Chem. Soc.*, 1963, 3097.

11 (*a*) M. Franceschin, L. Ginnari-Satriani, A. Alvino, G. Ortaggi and A. Bianco, *Eur. J. Org. Chem.*, 2010, **1**, 134; (*b*) L. Ji, Q. Fang, M.-S. Yuan, Z.-Q. Liu, Y.-X. Shen and H.-F. Chen, *Org. Lett.*, 2010, **12**(22), 5192.

12 E. M. García-Frutos, E. Gutierrez-Puebla, M. A. Monge, R. Ramírez, P. de Andrés, A. de Andrés, R. Ramírez and B. Gómez-Lor, *Org. Electron.*, 2009, **10**, 643.

13 G. Zhao, H. Dong, H. Zhao, L. Jiang, X. Zhang, J. Tan, Q. Meng and W. Hu, *J. Mater. Chem.*, 2012, **22**, 4409.

14 S. Wakim, J. Bouchard, M. Simard, N. Drolet, Y. Tao and M. Leclerc, *Chem. Mater.*, 2004, **16**, 4386.

15 P.-L. T. Boudreault, S. Wakim, N. Blouin, M. Simard, C. Tessier, Y. Tao and M. Leclerc, *J. Am. Chem. Soc.*, 2007, **129**, 9125.

16 (*a*) C. M. Cardona, W. Li, A. E. Kaifer, D. Stockdale and G. C. Bazan, *Adv. Mater.*, 2011, **23**, 2367; (*b*) A. J. Bard and L. R. Faulkner, *Electrochemical Methods: Fundamentals and Applications*, WILEY-VCH, New York, 2001.

